2026 34th Mediterranean Conference on Control and Automation (MED)
June 23-26, 2026. Ancona, Italy

An Observation-Oriented Optimal Finite Difference Discretization of the Single Particle Model

Andrea Autieri, Francesco Lo Iudice, *Member, IEEE*,
Simona Onori, *IEEE Fellow*, and Luigi Glielmo, *Senior Member, IEEE*

2026 34th Mediterranean Conference on Control and Automation (MED) | 979-8-3195-4746-0/26/$31.00 ©2026 IEEE | DOI: 10.1109/MED70602.2026.11598479

***Abstract*— In this paper, we consider the problem of optimizing the Finite Difference Method (FDM) discretization scheme of the Single Particle Model (SPM) for lithium ion batteries so to minimize the norm of the State of Charge (SoC) estimation error between a reduced and a full-order model. Specifically, we first recall the FDM discretization over a non uniform grid of the SPM. Then, we propose an algorithm to optimize the grid coordinates so to minimize the norm of the SoC estimation error produced by an extended Kalman Filter whose number of discretization points is much smaller than that of a baseline full-order model that is also affected by measurement and process noise. Our results indicate that optimizing the discretization scheme can lead to substantial reductions in the root mean square estimation error, attaining an optimal trade-off between accuracy and computational efficiency.**

I. Introduction

Lithium-ion batteries are the dominant energy storage technology in applications ranging from portable electronics to electric vehicles [1] and renewable energy systems [2]. To ensure safe and efficient operation, accurate estimation of the State of Charge (SOC) is essential. Since the SOC cannot be measured directly, it must be inferred from measurable input–output data through models and estimation algorithms.

Among the available approaches, model-based observers such as the Extended Kalman Filter (EKF) are widely adopted [3], [4], as they explicitly exploit battery dynamics and can operate under time-varying load conditions. Their performance, however, strongly depends on the accuracy, structure, observability, and computational complexity of the underlying battery model, which must remain compatible with real-time implementation in battery management systems.

To address this trade-off, reduced-order electrochemical models have been extensively investigated. In particular, the Single Particle Model (SPM) has emerged as a standard choice for SOC estimation, as it captures the dominant solid-phase diffusion dynamics while remaining significantly simpler than full physics-based models. Despite its reduced complexity, the SPM is governed by a diffusion partial differential equation (PDE) and therefore requires spatial discretization into a finite set of ordinary differential equations (ODEs) before it can be used for estimation purposes. As a consequence, the choice of discretization scheme and grid resolution directly affects model accuracy, physical consistency, and estimation performance.

Recent comparative studies have shown that different numerical discretization methods applied to electrochemical battery models may exhibit substantially different accuracy and robustness properties, even when derived from the same underlying continuous-time equations [5]. More generally, it has been shown that standard finite-difference discretization schemes for diffusion processes in spherical coordinates may fail to preserve mass, even in simple diffusion problems [6]. In the context of the SPM, [5] highlights that commonly used reduced-order finite-difference discretization schemes may violate lithium mass conservation, leading to nonphysical behavior over long operating horizons. This observation has motivated the study in [7], where two mass-preserving schemes, namely Finite Volumes and Control Volumes, are calibrated to optimize the trade-off between voltage root mean-square error—traditionally a weakness of these schemes—and computational complexity.

Beyond numerical accuracy and physical consistency, discretization choices also affect the observability properties of the discretized model. It has been shown that increasing the number of states may lead to a degradation of observability [8], and therefore does not necessarily improve estimation performance. A systematic analysis of the observability properties of different discretization schemes, as the number of internal states varies, is carried out in [9], where conclusive evidence is provided supporting the claim that observability is as relevant as accuracy and computational complexity when discretizing electrochemical models for observer design.

Taken together, these results indicate that the performance of SPM-based SoC estimation is strongly influenced by the spatial discretization itself, which should therefore be treated as a design element rather than a fixed modeling choice.

The aim of this work is to investigate whether the spatial grid of a finite-difference discretized SPM can be systematically designed to optimize the trade-off between model accuracy, observability, and computational burden for SoC estimation. To this end, non-uniform finite-difference discretizations are considered, and the grid node locations are optimized to minimize the SoC estimation error of an EKF based on a reduced-order model, evaluated with respect to a high-order reference discretization under realistic measurement and process noise.

To the best of our knowledge, only [10], [11] have previously explored the optimization of the SPM spatial

Andrea Autieri, Francesco Lo Iudice, and Luigi Glielmo are with the Department of Electrical Engineering and Information Technology, University of Naples Federico II, 80125 Naples, Italy.

Simona Onori is with the Department of Energy Science and Engineering, Stanford University, Stanford, CA, USA.

discretization. However, in these works the optimization is driven solely by model accuracy, that is, by the discrepancy between the reduced model and the full-order one. This naturally leads to multi-objective trade-offs in which improving the approximation of the internal state dynamics may be antithetic to accurately reproducing the output voltage. Moreover, the resulting observability properties of the optimized models are not investigated. By directly minimizing the SoC estimation error of a reduced-order EKF, and to the best of our knowledge for the first time in the SPM context, the approach proposed in this paper designs a discretization strategy that simultaneously accounts for model accuracy and observability.

II. The Single Particle Model

Before delving into the details of the SPM, let us define the notation used in this work. Given a vector x we will denote its i-th element as $[x]_i$, and consistently given a matrix X we will denote its ij-th element as $[X]_{i,j}$. Given a parameter or variable y_s, we will use the subscript $s \in \{p, n\}$ to indicate whether the y_s is associated to the positive or negative electrode. The parameters and nomenclature used in this work are given in Tables II and III in the Appendix.

The single particle model (SPM) is an electrochemical model of a battery cell that only focuses on lithium-ion diffusion in the solid phase. Each electrode $s = \{p, n\}$ is approximated by a single representative (or average) spherical particle. Within each particle s the radial diffusion is described by

$$\frac{\partial \vartheta_s(\rho,t)}{\partial t} = \frac{D_s}{R_s^2}\frac{1}{\rho^2}\frac{\partial}{\partial \rho}\left(\rho^2 \frac{\partial \vartheta_s(\rho,t)}{\partial \rho}\right), \tag{1}$$

where D_s is a diffusion coefficient, $\rho \in [0,\ 1]$ is the radial coordinate normalized to the particle radius R_s, $\vartheta_s(\rho,t)$ is the concentration of lithium ions normalized to the maximal possible concentration $c_{s,\max}$ in the respective electrode. Let the average ion flux $j_{\perp,s}(t)$, $s = p, n$, normal to the particle surface at the solid-solution boundary, averaged along the associated electrode, be

$$j_{\perp,s}(t) = \frac{-I(t)}{a_s \mathcal{F}\, \delta_s\, \varsigma}, \quad s \in \{p, n\}, \tag{2}$$

where $I(t)$ is the applied current, δ_s the electrode thickness, ς the sectional area of the cell, $\mathcal{F}$ Faraday's constant and a_s the electrode specific contact area. Then, we can give the boundary conditions accompanying equation (1):

$$\frac{\partial \vartheta_s(0,t)}{\partial \rho} = 0, \tag{3a}$$

$$\frac{\partial \vartheta_s(1,t)}{\partial \rho} = \pm \frac{R_s\, j_{\perp,s}(t)}{D_s\, c_{s,\max}} =: \beta_s(t). \tag{3b}$$

The $\pm$ sign is due to the ion flux exiting the negative electrode and entering the positive electrode in discharge and vice versa when the battery is charged; the $+$ sign applies to $s = p$ and the $-$ sign to $s = n$ during discharge. The quantity $\beta_s(t)$ is the normalized surface flux at the boundary of electrode s and plays the role of boundary forcing term entering the discretized state-space model derived in Section III. Finally, in the SPM the output voltage is modelled as

$$V(t) = U_p(\vartheta_p(1,t)) - U_n(\vartheta_n(1,t)) - R_\Omega\, I(t), \tag{4}$$

where R_Ω denotes a lumped ohmic resistance accounting for electrolyte, film, and contact resistive effects. The functions $U_p(\cdot)$ and $U_n(\cdot)$ are nonlinear maps of the surface concentrations whose form depends on the electrode materials under consideration, and are given in equations (26). A schematic representation of the Single Particle Model (SPM) architecture is provided in Figure 1.

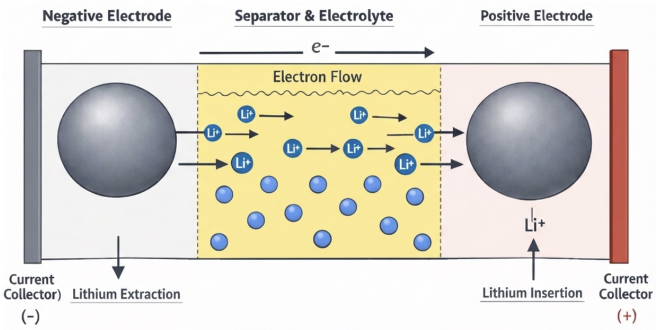

Fig. 1. Schematic representation of the Single Particle Model (SPM) adoption for a lithium-ion cell under discharge convention ($I > 0$). The model assumes instantaneous ionic diffusion within the electrolyte phase; therefore, the lithium ion flux exiting the negative electrode is assumed to immediately balance the flux entering the positive electrode. This strong assumption neglects concentration gradients and transport dynamics within the electrolyte, effectively treating it as a medium with infinite ionic conductivity.

III. FDM discretization over a non uniform grid

In what follows, we allow the positive and negative electrodes to be discretized over distinct non-uniform grids. For each electrode $s \in \{p, n\}$, the grid is described by the ordered vector of radial coordinates $\rho_s = [[\rho_s]_1, [\rho_s]_2, \ldots, [\rho_s]_{N_s}]^\top$ with $[\rho_s]_1 = 0$ and $[\rho_s]_{N_s} = 1$, where N_s is the number of grid points used for electrode s. We discretize equation (1) for each electrode via the finite differences method. The FDM spatial discretization scheme allows to approximate (1) for each electrode by a system of N_s linear ordinary differential equations

$$\frac{\mathrm{d}\theta_s(t)}{\mathrm{d}t} = F_s \theta_s(t) + B_s \beta_s(t), \quad s \in \{p, n\}. \tag{5}$$

whose output is the approximation of the voltage in (4)

$$V(t) = U_p([\theta_p]_{N_p}(t)) - U_n([\theta_n]_{N_n}(t)) - R_\Omega\, I(t), \tag{6}$$

In equations (5)–(6), $\theta_s(t) := [\theta_s(t)]_i$, $i = 1, \ldots, N_s$ is the state vector of each electrode with $[\theta_s]_i$ being the approximation generated by the discretized model of the normalized lithium concentration at node i, i.e., $\vartheta_s([\rho_s]_i, t)$. The term $B_s\beta_s(t)$ models the ion flux normal to the surface of the particle.

To apply the FDM, we first rewrite (1) as

$$\frac{\partial \vartheta_s(\rho,t)}{\partial t} = \frac{D_s}{R_s^2}\left(\frac{2}{\rho}\frac{\partial \vartheta_s(\rho,t)}{\partial \rho} + \frac{\partial^2 \vartheta_s(\rho,t)}{\partial \rho^2}\right), \tag{7}$$

and then approximate the first and second space derivatives of the normalized concentration at the internal node $[\rho_s]_i$ by combining the Taylor expansions of ϑ_s around $[\rho_s]_i$ evaluated at $[\rho_s]_{i-1}$ and $[\rho_s]_{i+1}$ and truncating at second order, which yields the standard three-point non-uniform stencils

$$\frac{\partial \vartheta_s([\rho_s]_i,t)}{\partial \rho} \approx \frac{[\theta_s]_{i+1}-[\theta_s]_{i-1}}{[\rho_s]_{i+1}-[\rho_s]_{i-1}}, \tag{8a}$$

$$\frac{\partial^2 \vartheta_s([\rho_s]_i,t)}{\partial \rho^2} \approx \frac{2}{[\rho_s]_{i+1}-[\rho_s]_{i-1}}\left(\frac{[\theta_s]_{i+1}-[\theta_s]_i}{[\rho_s]_{i+1}-[\rho_s]_i} - \frac{[\theta_s]_i-[\theta_s]_{i-1}}{[\rho_s]_i-[\rho_s]_{i-1}}\right). \tag{8b}$$

We note that, in the limit of uniform spacing, (8a)–(8b) reduce to the classical centered finite-difference formulas. Substituting (8) into (7) for $i=2,\dots,N_s-1$, we obtain the following expressions for the elements of the matrix F_s in equation (5) associated to the internal nodes:

$$[F_s]_{i,i-1} = \frac{2D_s/R_s^2}{[\rho_s]_{i+1}-[\rho_s]_{i-1}}\left(-\frac{1}{[\rho_s]_i}+\frac{1}{[\rho_s]_i-[\rho_s]_{i-1}}\right), \tag{9a}$$

$$[F_s]_{i,i} = -\frac{2D_s/R_s^2}{[\rho_s]_{i+1}-[\rho_s]_{i-1}}\left(\frac{1}{[\rho_s]_{i+1}-[\rho_s]_i}+\frac{1}{[\rho_s]_i-[\rho_s]_{i-1}}\right), \tag{9b}$$

$$[F_s]_{i,i+1} = \frac{2D_s/R_s^2}{[\rho_s]_{i+1}-[\rho_s]_{i-1}}\left(\frac{1}{[\rho_s]_i}+\frac{1}{[\rho_s]_{i+1}-[\rho_s]_i}\right). \tag{9c}$$

To obtain the expressions of the elements of F_s for nodes 1 and N_s we must consider the role of the boundary conditions (3). To do so, we consider two "ghost" nodes $i=0$ and $i=N_s+1$ and set $[\rho_s]_0=-[\rho_s]_2$ and $[\rho_s]_{N_s+1}=[\rho_s]_{N_s}+([\rho_s]_{N_s}-[\rho_s]_{N_s-1})$. Then, according to (3a) we enforce that (8a) is naught for $i=1$ yielding

$$[\theta_s]_2=[\theta_s]_0 \tag{10}$$

As $[\rho_s]_1=0$, substituting (10) in (8b) for $i=1$ we get

$$[F_s]_{1,2}=\frac{2D_s/R_s^2}{[\rho_s]_2^2}=-[F_s]_{1,1}. \tag{11}$$

For $\rho=1$, substituting the right hand side of (3b) into the left hand side of (8a) for $i=N_s$, we obtain

$$[\theta_s]_{N_s+1}=[\theta_s]_{N_s-1}+([\rho_s]_{N_s+1}-[\rho_s]_{N_s-1})\,\beta_s(t). \tag{12}$$

From (12) and since $[\rho_s]_{N_s+1}-[\rho_s]_{N_s-1}=2([\rho_s]_{N_s}-[\rho_s]_{N_s-1})$, the right hand side of (8b) for $i=N_s$ can be written as

$$\frac{2}{([\rho_s]_{N_s}-[\rho_s]_{N_s-1})^2}\left([\theta_s]_{N_s-1}-[\theta_s]_{N_s}-([\rho_s]_{N_s}-[\rho_s]_{N_s-1})\beta_s(t)\right). \tag{13}$$

Substituting (3b) and (13) in the right hand side of (7) yields

$$[F_s]_{N_s,N_s-1}=\frac{2D_s/R_s^2}{([\rho_s]_{N_s}-[\rho_s]_{N_s-1})^2}=-[F_s]_{N_s,N_s}. \tag{14}$$

Finally, (3a) and (13) also yield

$$[B_s]_{N_s}=\frac{2D_s}{R_s^2}\left(\frac{1}{[\rho_s]_{N_s}}+\frac{1}{[\rho_s]_{N_s}-[\rho_s]_{N_s-1}}\right). \tag{15}$$

IV. Grid optimization

In this section, we design an algorithm that attempts to optimize the nonuniform FDM discretization introduced in Section III so to minimize the root means square SoC estimation error. First of all, let us note that, for simplicity, we will consider a *half-cell* configuration, and only focus on the positive electrode, i.e., we will focus on $s=p$ and take $U_n(\vartheta_n(1,t))=0$ in (4). The half-cell configuration has been considered elsewhere in the literature for instance in the observability analyses conducted in [8]. Then, let us give the definition of SoC we will use, that is,

$$\mathrm{SoC}(t)=\frac{\bar\vartheta_{p,0}-\bar\vartheta_p(t)}{\bar\vartheta_{p,0}-\bar\vartheta_{p,100}} \tag{16}$$

where $\bar\vartheta_{p,0}$ and $\bar\vartheta_{p,100}$ are the normalized average lithium concentrations in the positive electrode when $\mathrm{SoC}(t)=0\%$ and $\mathrm{SoC}(t)=100\%$, respectively, while

$$\bar\vartheta_p(t)=\frac{1}{(4/3)\pi}\int_0^1 \vartheta_p(\rho,t)\,4\pi\rho^2 d\rho. \tag{17}$$

Equation (17) can be discretized as

$$\bar\theta_p(t)=\frac{1}{(4/3)\pi}\sum_{i=1}^{N_p}[\theta_p(t)]_i\,v_i, \tag{18}$$

where v_i is the fraction of the normalized particle volume associated to node i of the discretization grid. Hence

$$\widehat{\mathrm{SoC}}_q(t)=\frac{\bar\vartheta_{p,0}-\bar\theta_p(t)}{\bar\vartheta_{p,0}-\bar\vartheta_{p,100}} \tag{19}$$

is the approximation of the state of charge provided by a discretization over a grid of q points. Given this notation we can then define the SoC estimation root mean square error (RMSE) over a time window of T seconds as

$$\mathrm{RMSE}_{\mathrm{SoC}}=\sqrt{\frac{1}{T}\int_0^T\left(\mathrm{SoC}(t)-\widehat{\mathrm{SoC}}_q(t)\right)^2\mathrm{d}t}, \tag{20}$$

where the *true* $\mathrm{SoC}(t)$ is approximated using a *full* model, i.e., a FDM discretization of (1) over a uniform grid of $N_p^{\mathrm{full}}=80$ points, while $\widehat{\mathrm{SoC}}_q(t)$ is the SoC estimated by an EKF based on a q-point discretization with $q\ll N_p^{\mathrm{full}}$.

The overall estimation scheme used to compute the cost in (20) is depicted in Figure 2: the noisy voltage $\tilde V$, together with the applied current $I(t)$, drives the EKF based on the reduced q-node model, whose output $\widehat{\mathrm{SoC}}_q(t)$ is compared with the reference $\mathrm{SoC}(t)$ obtained from the full-order state via (18) to evaluate (20).

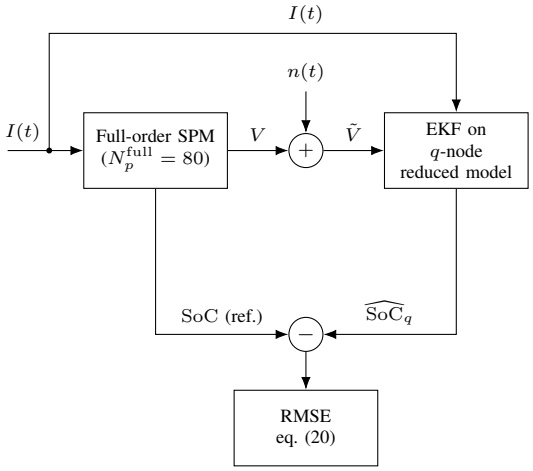

Fig. 2. Block diagram of the estimation scheme used to compute the cost in (20).

A. Optimization problem

Our algorithm aims at selecting the non-uniform grid point coordinate vector that solves

$$\min_{\rho_p} \; J(\rho_p) = \frac{\text{RMSE}_{\text{SoC}}^{6\text{A}}(\rho_p) + \text{RMSE}_{\text{SoC}}^{12\text{A}}(\rho_p)}{2}, \qquad (21)$$

where $\text{RMSE}_{\text{SoC}}^{I}(\rho_p)$ is the RMSE obtained by applying the constant current I and $\rho_p = [[\rho_p]_1, [\rho_p]_2, \ldots, [\rho_p]_q]^\top$ is the grid coordinate vector constrained by the following physically consistent conditions:

$$[\rho_p]_1 = 0, \qquad [\rho_p]_q = 1, \qquad (22)$$

$$[\rho_p]_1 < [\rho_p]_2 < \cdots < [\rho_p]_q, \qquad (23)$$

$$[\rho_p]_i - [\rho_p]_{i-1} \geq \delta_{\min}, \qquad i = 2, \ldots, q-1, \qquad (24)$$

with $\delta_{\min} = 0.02$ enforcing a minimum spacing between nodes. Equation (22) fixes the first and last nodes of the reduced grid at the particle centre and surface, respectively, so that the physical domain $[0, 1]$ is always fully covered. Equation (23) enforces a strictly increasing ordering of the internal nodes, ensuring a physically meaningful radial discretization without overlaps or inversions. Finally, equation (24) imposes a minimum distance $\delta_{\min}$ between consecutive nodes, which prevents excessively clustered grids and guarantees a well-conditioned discretization. Together, (21)–(24) define the complete grid-optimization problem.

B. Algorithm

Given q, the grid is optimized through the iterative local-search procedure reported in Algorithm 1, which terminates when the relative cost improvement falls below a tolerance ϵ or after $K_{\max}$ iterations.

Algorithm 1 Grid optimization for SPM-FDM EKF

Require: Number of nodes q, initial step Δ_0, tolerance ϵ, max iterations $K_{\max}$
Ensure: Optimized grid $\rho_p^\star$

Initialize $[\rho_p]_i \leftarrow (i-1)/(q-1)$ for $i = 1, \ldots, q$
$\Delta \leftarrow \Delta_0$; $k \leftarrow 0$; $J_k \leftarrow J(\rho_p)$
repeat
  `improved` $\leftarrow$ `false`
  for $i = 2, \ldots, q-1$ **do**
    for $\sigma \in \{+1, -1\}$ **do**
      $\rho_p^{\text{trial}} \leftarrow \rho_p$; $[\rho_p^{\text{trial}}]_i \leftarrow [\rho_p]_i + \sigma\Delta$
      if ρ_p^{trial} satisfies (22)–(24) **and** $J(\rho_p^{\text{trial}}) < J(\rho_p)$ **then**
        $\rho_p \leftarrow \rho_p^{\text{trial}}$; `improved` $\leftarrow$ `true`
      end if
    end for
  end for
  if not `improved` **then**
    $\Delta \leftarrow \frac{1}{2}\Delta$
  end if
  $k \leftarrow k + 1$; $J_k \leftarrow J(\rho_p)$
until $|J_k - J_{k-1}|/J_{k-1} < \epsilon$ **or** $k \geq K_{\max}$
return $\rho_p^\star \leftarrow \rho_p$

V. Numerical testing

A. Optimization set-up

In this section we aim to investigate whether the methods presented in Sections III and IV can help improve the trade-off between model accuracy, observability and computational complexity. To this aim, we run the optimization algorithm in Section IV for $q \in \{3, \ldots, 12\}$. From a numerical point of view, $q = 3$ is the minimum value that still allows a sensible approximation of the concentration profile inside the particle. Smaller values would lead to an overly coarse discretization, with a clearly insufficient accuracy for the estimator. Preliminary computations of the root mean square error in (20) over a uniform grid and varying q in the range $3, \ldots, 12$ showed that the error decreases as q increases, but with diminishing returns. In particular, the behavior for $q = 9$, 10, 11, is very similar to the case of $q = 12$, suggesting that considering values of q greater than 12 would be unnecessary. Throughout the optimization, we set $T = 2160\,\text{s}$ for the 6 A (1C) discharge and $T = 1080\,\text{s}$ for the 12 A (2C) discharge, and discretize in time with a constant sampling interval $\Delta t = 0.1\,\text{s}$. The values $I = 6\,\text{A}$ (1C) and $I = 12\,\text{A}$ (2C) cover both a moderate and a more demanding operating regime; averaging the two RMSE values in (21) prevents the optimized grid from over-fitting to a single C-rate. The full-order reference simulation (uniform FDM with $N_p^{\text{full}} = 80$) is initialized at $\text{SoC}(0) = 0.8$ by setting uniform solid concentrations inside each particle, i.e., $\theta_p(0) = \theta_{p,80}\mathbf{1}_{80}$ and $\theta_n(0) = \theta_{n,80}\mathbf{1}_{80}$, where $\theta_{p,80}$ and $\theta_{n,80}$ are the normalized concentrations corresponding to 80% SoC in the adopted parameter set, and $\mathbf{1}_{80}$ is a vector of dimension 80 and all elements equal to 1. The EKF is implemented in a windowed fashion; therefore, at

the beginning of each time window the reduced model state is initialized by interpolating the full-order concentration profile onto the q-node grid ρ_p and adding a small random perturbation (with independent components uniformly distributed in $[-0.02, 0.02]$), consistently for all tested grids. We corrupt the output of the full order model with measurement noise, i.e., we assume that the *true* measured voltage is

$$\tilde{V}(k\Delta t) = U_p([\theta_p(k\Delta t)]_{80}) + n(k\Delta t), \tag{25}$$

where $n(k\Delta t)$ is a zero-mean white Gaussian noise with standard deviation $\sigma_V = 0.01\, V_{\text{nom}}$, i.e., $\text{Var}(n) = \sigma_V^2 = (0.01\, V_{\text{nom}})^2 = 10^{-4} V_{\text{nom}}^2$. Finally, to mimic the realistic case where the input current measurement slightly differs from the current actually fed to the battery, we assume that the discrete-time dynamics of the surface concentration of the full order model $[\theta_p]_{80}(k\Delta t)$ is affected by an additive white process noise of variance $Q = (0.01\, I)^2$.

For each value of q we solve the same optimization problem defined in IV-A, with the cost $J(\rho_p)$ defined as in (21), i.e., measuring the discrepancy between the reduced model and the reference model (with $N = 80$ nodes) over two discharge cycles, one at $I = 6$A, that is 1C, and one at $I = 12$A, i.e., 2C. For each value of q we denote by J_0 the value of the cost associated with the uniform (reduced) grid and by $J^\star$ the optimal value achieved after the grid optimization. The relative reduction is defined as

$$\frac{\Delta J}{J_0} = \frac{J_0 - J^\star}{J_0} \cdot 100\%.$$

B. Results

Table I summarizes the results for each value of q except $q \in \{9, 10, 11\}$ for brevity. The column "Ops./step" reports the number of floating-point operations per EKF step, computed for the half-cell estimator with scalar measurement output and banded state-transition matrix F_s, exploiting the tridiagonal sparsity of F_s under a Forward Euler discretization $F_s^d \approx I + \Delta t\, F_s$.

TABLE I
GRID OPTIMIZATION RESULTS (UNIFORM INITIALIZATION, $Q \neq 0$).

q	J_0	$J^\star$	$\Delta J/J_0$	Ops./step
3	$5.371 \cdot 10^{-2}$	$4.951 \cdot 10^{-2}$	7.8%	142
4	$4.682 \cdot 10^{-2}$	$3.905 \cdot 10^{-2}$	16.6%	249
5	$4.300 \cdot 10^{-2}$	$3.384 \cdot 10^{-2}$	21.3%	386
6	$4.034 \cdot 10^{-2}$	$3.050 \cdot 10^{-2}$	24.4%	553
7	$3.859 \cdot 10^{-2}$	$2.807 \cdot 10^{-2}$	27.2%	750
8	$3.588 \cdot 10^{-2}$	$2.580 \cdot 10^{-2}$	28.1%	977
12	$2.999 \cdot 10^{-2}$	$2.076 \cdot 10^{-2}$	30.8%	2185

As the number of nodes q increases, the optimized cost $J^\star$ decreases and the relative reduction $\Delta J/J_0$ improves. In other words, using more radial nodes always enhances the performance of the extended Kalman Filter suggesting that increase in model accuracy prevails over the decrease in model observability at least for $q \leq 12$. However the effectiveness of optimizing the discretization grid is striking. Indeed it allows to substantially reduce the model complexity while preserving the same accuracy. For instance, an optimized nonuniform grid with $q = 4$ points allows the corresponding EKF to match the performance of an EKF based on a uniform grid of $q = 7$ points. At the same time, the trend in the marginal decreases of the cost function J with q is clear: the percentage reduction in J obtained when moving from $q = 4$ to $q = 8$ is almost double than that obtained when moving from $q = 8$ to $q = 12$.

Figure 3 shows the corresponding radial grids. Each panel contains two subplots: on the left, the initial uniform grids; on the right, the optimized grids obtained by the local search.

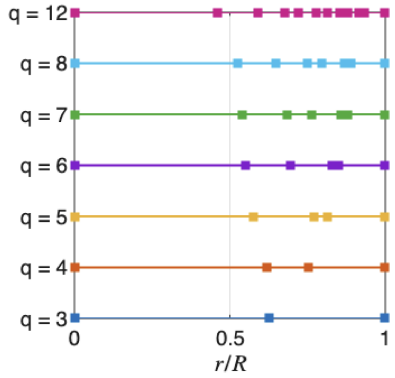

Fig. 3. Optimized grids for $q = 3, \ldots, 8, 12$ with process noise $Q \neq 0$ and uniform initialization.

In all optimized configurations, the internal nodes are progressively shifted towards the particle surface (larger values of ρ), while the core region is represented with fewer points. This effect is clearly visible in Fig. 3: for each q, the optimized markers are denser in the interval $[0.5, 1]$ and sparser in the interval $[0, 0.5]$. This behavior suggests that model observability is enhanced by concentrating the grid points toward the surface so to better estimate the terminal voltage, as the latter is a function of the surface concentration. In this sense, the reduction $\Delta J/J_0$ of the cost reported in Table I is not only a global improvement of the model accuracy, but is also achieved by allocating more resolution to the part of the state that is effectively more observable by the EKF.

While the choice of the reduced model order depends on the computational budget available on the target BMS, the operation count in Table I shows that moving from $q = 8$ to $q = 12$ more than doubles the per-step arithmetic cost (977 to 2185 operations, $+124\%$) while yielding only a marginal improvement in $J^\star$ ($+24\%$ reduction). Our results therefore indicate $q = 8$ as a well-defined knee point in the accuracy–complexity trade-off.

VI. CONCLUSIONS

In this work, we investigate whether a non uniform finite difference discretization of the Single Particle Model can be exploited so optimize the trade-off between computational burden and performance of the SoC estimation task in lithium

ion batteries via electrochemical models. To this aim, we first derive a non-uniform FDM discretization of the SPM and then optimize the grid point coordinates so to minimize the root mean square of the SoC estimation error produced by an Extended Kalman Filter based on the aforementioned discretization. Unlike previous SPM grid-optimization approaches, which rely on model-accuracy criteria only, the proposed scheme directly targets the SoC estimation error of the reduced-order EKF, thereby implicitly accounting for the observability of the discretized model. Altogether, our results indicate that exploiting an optimal grid can allow to reduce the model complexity by almost 50% (i.e. use half the number of discretization points), while preserving the same level of performance.

VII. Appendix. Parameters and open circuit potentials

In this work, we use the parametrization of the SPM taken from [12]–[14] and given in Table II.

TABLE II
PARAMETERS

Description	Symbol	Value
Solid phase Li^+ diffusivity	D_n	2×10^{-12} cm^2 s^{-1}
	D_p	3.7×10^{-12} cm^2 s^{-1}
Representative particle radius	R_n	1×10^{-4} cm
	R_p	1×10^{-4} cm
Specific interfacial surface area	a_n	17400 cm^{-1}
	a_p	15000 cm^{-1}
Electrode / separator thickness	δ_n	50×10^{-4} cm
	δ_{sep}	25.4×10^{-4} cm
	δ_p	36.4×10^{-4} cm
Sectional cell area	ς_s	10452 cm^2
Film resistance at interphase	R_f	20 Ω cm^2
Maximum Li^+ concentration	$c_n^{\max}$	16.1×10^{-3} mol cm^{-3}
	$c_p^{\max}$	23.9×10^{-3} mol cm^{-3}
Stoichiometry at 0% SoC	θ_n^0	0.126
	θ_p^0	0.936
Stoichiometry at 100% SoC	θ_n^{100}	0.676
	θ_p^{100}	0.442
Faraday's constant	F	96487 C mol^{-1}

As for the output function we set

$$\begin{aligned} U_p\left(\vartheta_p(1,t)\right) &= 85.681\,\vartheta_p^6 - 357.70\,\vartheta_p^5 + 613.89\,\vartheta_p^4 \\ &\quad - 555.65\,\vartheta_p^3 + 281.06\,\vartheta_p^2 - 76.648\,\vartheta_p + 13.1983 \\ &\quad - 0.30987\exp\left(5.657\vartheta_p^{115}\right), \end{aligned} \tag{26a}$$

$$\begin{aligned} U_n\left(\vartheta_n(1,t)\right) &= 8.00229 + 5.0647\,\vartheta_n - 12.5780\,\vartheta_n^{1/2} \\ &\quad - 8.6322 \times 10^{-4}\,\vartheta_n^{-1} + 2.1765 \times 10^{-5}\,\vartheta_n^{3/2} \\ &\quad - 0.46016\exp\left[15\left(0.06 - \vartheta_n\right)\right] \\ &\quad - 0.55364\exp\left[-2.4326\left(\vartheta_n - 0.92\right)\right]. \end{aligned} \tag{26b}$$

TABLE III
NOMENCLATURE

Symbol	Description
s	Electrode index, $s \in \{p, n\}$
ρ	Normalized radial coordinate, $\rho \in [0, 1]$
$\vartheta_s(\rho, t)$	Dimensionless solid-phase lithium concentration
$\theta_s(t)$	Discrete concentration state vector, $\theta_s(t) \in \mathbb{R}^{N_s}$
N_s	Number of spatial nodes for electrode s
N_p^{full}	Number of nodes of the full-order reference model
q	Number of nodes of the reduced-order model
ρ_s	Non-uniform grid vector for electrode s
$\beta_s(t)$	Boundary forcing term associated with surface lithium flux
$\bar{\vartheta}_p(t)$	Average normalized lithium concentration (positive electrode)
$\bar{\theta}_p(t)$	Discrete approximation of $\bar{\vartheta}_p(t)$
$\text{SoC}(t)$	State of Charge
$\widehat{\text{SoC}}_q(t)$	EKF-based SoC estimate using q nodes
RMSE_{SoC}	Root mean square SoC estimation error
$J(\rho_p)$	Grid optimization cost function
$n(k\Delta t)$	Voltage measurement noise
σ_V	Voltage noise standard deviation
Q	Process noise variance

References

[1] F. Naseri, S. Gil, C. Barbu, E. Çetkin, G. Yarimca, A. Jensen, P. G. Larsen, and C. Gomes, "Digital twin of electric vehicle battery systems: Comprehensive review of the use cases, requirements, and platforms," *Renewable and Sustainable Energy Reviews*, vol. 179, p. 113280, 2023.

[2] J. Arteaga, H. Zareipour, and V. Thangadurai, "Overview of lithium-ion grid-scale energy storage systems," *Current Sustainable/Renewable Energy Reports*, vol. 4, no. 4, pp. 197–208, 2017.

[3] C. Lin, A. Tang, and J. Xing, "Evaluation of electrochemical models based battery state-of-charge estimation approaches for electric vehicles," *Applied Energy*, vol. 207, pp. 394–404, 2017.

[4] D. Zhang, L. D. Couto, and S. J. Moura, "Electrode-level state estimation in lithium-ion batteries via kalman decomposition," *IEEE Control Systems Letters*, vol. 5, no. 5, pp. 1657–1662, 2020.

[5] L. Xu, J. Cooper, A. Allam, and S. Onori, "Comparative analysis of numerical methods for lithium-ion battery electrochemical modeling," *Journal of The Electrochemical Society*, vol. 170, no. 12, p. 120525, 2023.

[6] A. N. Ford Versypt and R. D. Braatz, "Analysis of finite difference discretization schemes for diffusion in spheres with variable diffusivity," *Computers & Chemical Engineering*, vol. 71, pp. 241–252, 2014.

[7] J. N. E. Lucero, L. Xu, and S. Onori, "Comparing mass-preserving numerical methods for the lithium-ion battery single particle model," in *2024 Modeling, Estimation and Control Conference (MECC)*. IEEE, 2024.

[8] A. Allam and S. Onori, "Linearized versus nonlinear observability analysis for lithium-ion battery dynamics: Why respecting the nonlinearities is key for proper observer design," *IEEE Access*, vol. 9, pp. 163 431–163 440, 2021.

[9] J. N. Lucero and S. Onori, "Comparative nonlinear observability analysis of spatial discretization schemes for lithium-ion battery models," in *2025 American Control Conference (ACC)*. IEEE, 2025, pp. 2805–2810.

[10] T.-K. Lee and Z. S. Filipi, "Electrochemical li-ion battery modeling for control design with optimal uneven discretization," in *Dynamic Systems and Control Conference*, vol. 54754, 2011, pp. 493–500.

[11] I. Oyewole, K. H. Kwak, Y. Kim, and X. Lin, "Optimal discretization approach to the enhanced single-particle model for li-ion batteries," *IEEE Transactions on Transportation Electrification*, vol. 7, no. 2, pp. 369–381, 2020.

[12] A. Romero-Becerril and L. Alvarez-Icaza, "Comparison of discretization methods applied to the single-particle model of lithium-ion batteries," *Journal of Power Sources*, vol. 196, no. 23, pp. 10 267–10 279, 2011.

[13] K. A. Smith, C. D. Rahn, and C.-Y. Wang, "Control oriented 1d electrochemical model of lithium ion battery," *Energy Conversion and management*, vol. 48, no. 9, pp. 2565–2578, 2007.

[14] K. Smith and C.-Y. Wang, "Solid-state diffusion limitations on pulse operation of a lithium ion cell for hybrid electric vehicles," *Journal of power sources*, vol. 161, no. 1, pp. 628–639, 2006.